ORIGINAL RESEARCH ARTICLE

Effect of Ni on Microstructures and Mechanical Properties for Multielemental Nb–Si-Based Alloys

DEZHI CHEN, QI WANG, RUIRUN CHEN, ZHECHENG ZHOU, YANQING SU, and HENGZHI FU

Eight-element Nb–Si alloys (Nb–Si–Ti–Cr–Al–Hf–Zr–Ni) with different Ni contents were prepared by arc melting to obtain Nb–Si alloys with high mechanical properties. Phase selection, microstructure evolution, room-temperature fracture toughness, and compressive properties were investigated systematically. Results showed that the eutectic Nb–Si alloy becomes a hypereutectic Nb–Si alloy with the increase in Ni content. All alloys contain Nbss, γ-(Nb, X)$_5$Si$_3$ and Cr$_2$(Nb, X) phases, and 2Ni and 3Ni alloys also contain the primary α-(Nb, X)$_5$Si$_3$ phase. With the increase in Ni content, the content and size of the primary α-(Nb, X)$_5$Si$_3$ phase increased. K_Q first increased and then decreased, with the highest K_Q of 12.6 MPa m$^{1/2}$ occurring in the 2Ni alloy. The room-temperature maximum compressive strength was improved with 1 at. pct Ni addition but decreased with higher Ni addition. The strengthening mechanism is solid solution strengthening and a high content of the γ-(Nb, X)$_5$Si$_3$ phase by Ni element addition.

https://doi.org/10.1007/s11661-022-06634-0
© The Minerals, Metals & Materials Society and ASM International 2022

I. INTRODUCTION

DUE to their high melting point (excess 1750 °C), low density (6.6 to 7.4 g/cm^3), and thermal stability, Nb–Si-based alloys have become the most promising high-temperature structural materials, such as turbine engine blade components.[1] If the nickel-base superalloy is replaced with a Nb–Si-based alloy in an advanced engine that is currently in service, the rotor weight will decrease by more than 20 pct.[2] Nb–Si-based alloys contain two phases: a ductile phase Niobium solid solution (Nbss) and a strengthening phase silicide. The ductile phase provides the room-temperature fracture toughness, while the silicide phase provides high strength, stiffness, and creep resistance.[3] Silicides contain four types, α-Nb$_5$Si$_3$ (D8$_1$, *tI*32 Cr$_5$B$_3$-type), β-Nb$_5$Si$_3$ (D8m, *tI*32 W$_5$B$_3$-type), Nb$_3$Si (*tP*32 PTi$_3$-type), and metastable phase γ-Nb$_5$Si$_3$ (D8$_8$, *hP*16 Mn$_5$B$_3$-type).[4,5] Body-centered tetragonal α-Nb$_5$Si$_3$ is a low-temperature stable phase, while body-centered tetragonal β-Nb$_5$Si$_3$ is a high-temperature stable phase. Elements such as Zr, Hf, and Ti can stabilize the hexagonal γ-Nb$_5$Si$_3$ phase,[6,7] and Nb$_3$Si decomposes into Nbss and silicide through a eutectoid reaction (Nb$_3$Si $\rightarrow$ Nbss + α-Nb$_5$Si$_3$).[8] However, this transformation is sluggish in nature. The enthalpy values of formation of the three silicides are α-Nb$_5$Si$_3$, β-Nb$_5$Si$_3$, and γ-Nb$_5$Si$_3$ in descending order.[9] The β-Nb$_5$Si$_3$ and γ-Nb$_5$Si$_3$ phases can be stabilized at room temperature through elements. For example, Co, Mo, and Ge can stabilize β-Nb$_5$Si$_3$, and Cr, Hf, and Zr can stabilize the γ-Nb$_5$Si$_3$ phase at room temperature.[10–13] Also, β-Nb$_5$Si$_3$ can be transformed into α-Nb$_5$Si$_3$ in some Nb–Si alloys via high-temperature heat treatment. Zhang and Guo[11] reported that a relatively complete transformation from β-Nb$_5$Si$_3$ to α-Nb$_5$Si$_3$ occurred during heat treatment (1450 °C/50 h) in a Nb–22Ti–16-Si–3Al alloy. Kim *et al.*[14] reported that Mo can stabilize the β-Nb$_5$Si$_3$ phase. The room-temperature microstructure of the Nb-(18, 22) Si-(5, 15) Mo alloy by arc smelting is β-Nb$_5$Si$_3$ + Nbss. After 1850 °C for 48 h, the β-Nb$_5$Si$_3$ phase transforms into α-Nb$_5$Si$_3$. Li and Tsakiropoulos[15] reported that Nb–16Si–(5, 10) Ge alloy can undergo a β-Nb$_5$Si$_3$ to α-Nb$_5$Si$_3$ transformation after 1500 °C for 100 hours.

Insufficient room-temperature fracture toughness is an essential obstacle to the application of Nb–Si-based alloys. The fracture toughness of the monolithic Nb$_5$Si$_3$ phase is (1 to 3) MPa·m$^{1/2}$.[16,17] The Nbss phase can markedly improve room-temperature fracture toughness. At the tail of the crack propagation, the Nbss phase reduces the crack tip stress intensity factor and

DEZHI CHEN and ZHECHENG ZHOU are with the National Key Laboratory for Precision Hot Processing of Metals, Harbin Institute of Technology, Harbin, China. QI WANG, RUIRUN CHEN, YANQING SU, and HENGZHI FU are with the National Key Laboratory for Precision Hot Processing of Metals, Harbin Institute of Technology and also with the School of Materials Science and Engineering, Harbin Institute of Technology, Harbin 150001, China. Contact e-mails: wangqi_hit@163.com; ruirunchen@hit.edu.cn
Manuscript submitted August 27, 2021; accepted February 11, 2022. Article published online March 8, 2022

even traps the crack, thereby increasing the fracture resistance curve.[14] Recent studies have shown that microcracks in silicide phases with moderate sizes can induce crack deflection and even create secondary cracks.[13] Crack tip blunting, crack deflection, trapping, and bridging, or a combination of these processes, are all instances of *in situ* composite toughening.[18,19]

Alloying elements can affect the chemical composition, size, volume fraction of the continuous phase (Nbss and silicide), and mechanical properties.[20,21] To date, the six-element Nb–Si–Ti–Cr–Al–Hf alloy system has been investigated in the most detail.[7,13] Ti and Hf elements have been shown to be beneficial to both room-temperature fracture toughness and high-temperature oxidation resistance.[1,4] Ti and Hf elements can improve room-temperature fracture toughness because they reduce the energy barriers of DBTT and Peierls–Nabarro (P–N) barrier energy and increase the divergence of crack tip dislocations.[16,22] Oxidation resistance is improved because Ti and Hf elements enhance the composition and adhesion of the oxide film and inhibit the diffusion of oxygen atoms.[23,24] Cr promotes the formation of the Cr_2Nb phase, thus inhibiting oxygen diffusion and improving oxidation resistance.[25,26] Due to its high activity, Al forms a dense Al_2O_3 layer on the surface, hindering oxygen diffusion and improving oxidation resistance.[27,28] According to Zelenitsas and Tsakiropoulos,[29] the microstructures of Nb–24Ti–18Si–5Al and Nb–24Ti–18Si–5Cr–5Al alloys are composed of the Nbss and β-Nb_5Si_3 phases. Al promotes precipitation of the Cr-rich C_{14} Laves phase around the (Nb, Ti)ss grains in the heat-treated Nb–24Ti–18Si–5Cr–5Al and Nb–24Ti–18Si–8Cr–4Al alloys. Kashyap *et al.*[30] reported that Al could refine the eutectic structure, improve room-temperature fracture toughness, and promote the precipitation of the δ-$Nb_{11}Si_4$ phase, thereby improving high-temperature performance. The improvement in fracture toughness is attributed to the substitution of Si by metallic Al in Nb_5Si_3.[31] Many studies have shown that Zr can improve room-temperature fracture toughness and oxidation resistance in ternary, quaternary, or seven-element alloys.[32–36] Therefore, this study adds Zr to six-element alloys and finally identifies a Nb–Si–Ti–Cr–Al–Hf–Zr seven-element system alloy with better mechanical properties as the base alloy.

To our knowledge, few studies have investigated Ni elements for Nb–Si alloys.[37,38] Also, there has been no systematic research on multielemental Nb–Si alloys with different Ni contents. Thus, the focus of this study was to systematically investigate the influence of different Ni contents on the microstructure and mechanical properties of Nb–Si–Ti–Cr–Al–Hf–Zr-based alloys. The optimal Ni content can be obtained in a multielemental Nb–Si alloy, which will set the groundwork for Nb–Si alloy applications.

II. EXPERIMENTAL PROCEDURE

Four alloys with nominal compositions Nb–16Si–20Ti–4Cr–1.5Al–4Hf–4Zr–xNi (x = 0, 1, 2, and 3 at. pct) were prepared by non-consumable electrode arc melting using a copper water-cooled crucible, as shown in Table I. Each prefabricated alloy ingot had a mass of 120 g with a weight loss rate of less than 0.5 pct. The ingot size prepared by melting was approximately 53 mm in diameter and approximately 11 mm in maximum thickness. In this paper, the alloys are represented by 0Ni, 1Ni, 2Ni, and 3Ni. The 0Ni alloy was a base alloy that contrasts with other alloys of different Ni contents in microstructure and mechanical properties. The raw materials used in this study were 99.95 wt pct Nb block (3 to 8 μm), 99.99 wt pct Si block (5 to 10 μm), 99.4 wt pct Ti sponge (3 to 10 μm), 99.95 wt pct Al particles (Ø3 × 3 μm), 99.7 wt pct Cr blocks (1 to 3 μm), 99.7 wt pct Hf blocks (1 to 3 μm), 99.4 wt pct Zr particles (Ø3×3 μm), and Ni particles – 99.9 wt pct (Ø3×3 μm). Each alloy ingot was melted six times to ensure homogeneity.

Samples for microstructure observation and room-temperature mechanical performance testing were prepared by electrodischarge machining (EDM). All samples were mechanically polished by SiC abrasive paper and then polished to achieve a mirror-finish surface before the test. The three-point bending specimen was 20 mm (length) × 4 mm (height) × 2 mm (thickness). The notch (2 mm) was prefabricated in the middle of the three-point bending sample using a Mo wire diameter of 0.2 mm. According to ASTM E399,[39] the universal testing machine Instron 5569 was used with an initial cross-head speed of 0.2 mm/min at room temperature, and the experiment was performed at a span of 16 mm. The size of the compressed sample at room temperature was Ø4 × 6, and the compression rate was 0.5 mm/min. All mechanical property test specimens were tested three times, and the average value was calculated.

The phases were detected by X-ray diffraction (PANalytical, XRD, Empyrean) using CuKα radiation at an 8°/min scanning speed. The microstructures and the chemical compositions of the alloys were analyzed by quanta 200FEG in backscattered electron (BSE) mode and energy-dispersive X-ray spectroscopy (EDS). The 200FEG measured the fracture topography of three-bending samples in secondary electron mode. The chemical compositions of all ingots are listed in Table II and were obtained by wave-dispersive spectroscopy (EPMA, JXA-8230). The three measurement areas were all 3 μm × 3 μm. Results show that the composition of all ingots is basically the same as the nominal composition. 3D measuring laser microscopy was used to investigate the three-dimensional morphologies of alloy fracture surfaces (LEXT OLS4100). The volume fraction of the continuous phase was measured using Image-Pro Plus 6.0 software.

III. RESULTS

A. *Phase Identification by XRD*

Figure 1 shows the XRD patterns of multielemental Nb–Si alloys with different Ni contents. All alloys contain Nbss and γ-$(Nb, X)_5Si_3$ phases, where X

represents the substitution of Ti, Zr, and Hf elements for Nb and the 2Ni and 3Ni alloys have a diffraction peak corresponding to the α-(Nb, X)$_5$Si$_3$ phase. The phase compositions of the 0Ni and 1Ni alloys were the same: only Nbss and γ-(Nb, X)$_5$Si$_3$. In contrast, 2Ni and 3Ni alloys contained three phases: Nbss, α-(Nb, X)$_5$Si$_3$ and γ-(Nb, X)$_5$Si$_3$. Adding 1 at. pct Ni to the phase composition had little effect, while adding more than 2 at. pct Ni facilitated the formation of α-(Nb, X)$_5$Si$_3$. Furthermore, there was no metastable Nb$_3$Si phase in all alloys, indicating that adding multiple elements could promote the decomposition of the Nb$_3$Si phase.

The lattice parameters of the phases in all alloys are listed in Table III by the Rietveld method and MDI Jade 6.0 software. The lattice parameter of the Nbss phase decreased from 3.2908 to 3.2884 Å with the addition of Ni. The primary reason for this decrease in the lattice constant was the Ni solid solution in the Nbss phase. Ni has a small atomic radius element (r_{Ni} = 0.125 nm < r_{Nb} = 0.143 nm).[40] In the 1Ni alloy, the c/a value of the γ-(Nb, X)$_5$Si$_3$ phase was marginally higher than that in 0Ni. The c/a value of the γ-(Nb, X)$_5$Si$_3$ phase remained essentially unaltered as the Ni content exceeded 1 at. pct. The c/a value of the α-(Nb, X)$_5$Si$_3$ phase increased from 1.7911 to 1.8053 with the increase in Ni content.

B. *Microstructure*

Figure 2 shows the BSE images of multielemental Nb–Si alloys with different Ni contents. The chemical composition of the continuous phase in all alloys is listed in Table IV. Four phases of white, gray, black, and light gray are shown in the microstructure in Figure 2. According to Section III–A and EDS analysis, the white phase was Nbss, the gray phase was γ-(Nb, X)$_5$Si$_3$, the black phase was Cr$_2$(Nb, X), and the light gray phase is α-(Nb, X)$_5$Si$_3$. Because the area of the black phase was small, the diffraction peak of Cr$_2$(Nb, X) was not found in the XRD pattern.

0Ni is a eutectic alloy [Nbss/γ-(Nb, X)$_5$Si$_3$] because there is no sizeable primary phase. Nbss phases are primarily rod-like and nearly elliptical morphologies; γ-(Nb, X)$_5$Si$_3$ phases are primarily irregularly long strips or connected as a network. The 0Ni alloy also contained a certain amount of lamellar eutectic structure, and the thickness of lamellar γ-(Nb, X)$_5$Si$_3$ was only approximately (1 to 3) μm, as illustrated in Figure 2(b). The Cr$_2$(Nb, X) phase was primary distributed at the edge of the eutectic cluster or at the phase boundary between Nbss and γ-(Nb, X)$_5$Si$_3$. The microstructure of the 1Ni alloy is shown in Figure 2(c) and was similar to the 0Ni alloy as a eutectic structure without a primary phase and consisted of Nbss, γ-(Nb, X)$_5$Si$_3$, and Cr$_2$(Nb, X).

In contrast to the 0Ni and 1Ni alloys, the 2Ni alloy generated many α-(Nb, X)$_5$Si$_3$ phases with sizes ranging from 20 to 50 μm. The morphology of the α-(Nb, X)$_5$Si$_3$ phases was primarily island-shaped, and EDS results show that the Ti concentration of the α-(Nb, X)$_5$Si$_3$ phase was only 10 pct, which was two-thirds of that in γ-(Nb, X)$_5$Si$_3$. The 2Ni alloy had an anomalous eutectic structure with an island-like γ-(Nb, X)$_5$Si$_3$ distributed on the Nbss matrix. The island-like γ-(Nb, X)$_5$Si$_3$ phase ranged from several to tens of microns.

With the addition of more Ni, a larger α-(Nb, X)$_5$Si$_3$ phase with a length of up to 200 μm appeared in the 3Ni alloy. The shape of α-(Nb, X)$_5$Si$_3$ was primarily rod-like and regular quadrilateral. The primary α-(Nb, X)$_5$Si$_3$ phase had a typical non-faceted dendritic morphology, which was different from γ-(Nb, X)$_5$Si$_3$. 2Ni and 3Ni alloys are hypereutectic alloys with primary α-(Nb, X)$_5$Si$_3$ phases due to the presence of a large number of continuous phases [α-(Nb, X)$_5$Si$_3$] with a size of more than 20 μm. These results indicate that adding Ni to multielemental Nb–Si alloys influenced the solidification path, resulting in the precipitation of the primary α-(Nb, X)$_5$Si$_3$ phase.

Figures 2(d) and (h) show microcracks in the γ-(Nb, X)$_5$Si$_3$ phase but none in the α-(Nb, X)$_5$Si$_3$ phase. The primary reason for this results is that the γ-(Nb, X)$_5$Si$_3$ phase is a hexagonal crystal, while the α-(Nb, X)$_5$Si$_3$ phase is a tetragonal crystal.[4] Therefore, compared with the γ-(Nb, X)$_5$Si$_3$ phase, the α-(Nb, X)$_5$Si$_3$ phase contained more slip systems.[41] Thus, the formation of the α-(Nb, X)$_5$Si$_3$ phase rather than the γ-(Nb, X)$_5$Si$_3$

Table I. Nominal Compositions of All Alloys With Different Ni Contents

Alloy	Composition (At. Pct)							
	Nb	Si	Ti	Cr	Al	Hf	Zr	Ni
0Ni	50.5	16	20	4	1.5	4	4	0
1Ni	49.5	16	20	4	1.5	4	4	1
2Ni	48.5	16	20	4	1.5	4	4	2
3Ni	47.5	16	20	4	1.5	4	4	3

Table II. Chemical Compositions of all Alloys With Different Ni Contents

Alloy	Composition (At. Pct)							
	Nb	Si	Ti	Cr	Al	Hf	Zr	Ni
0Ni	48.3 ± 0.2	17.8 ± 0.1	20.1 ± 0.3	3.9 ± 0.1	1.4 ± 0.1	4.2 ± 0.2	4.3 ± 0.2	—
1Ni	47.4 ± 0.3	17.6 ± 0.2	20.2 ± 0.2	3.8 ± 0.2	1.3 ± 0.2	4.3 ± 0.1	4.4 ± 0.1	1.0 ± 0.1
2Ni	45.8 ± 0.1	17.8 ± 0.2	20.4 ± 0.2	3.9 ± 0.2	1.3 ± 0.1	4.4 ± 0.1	4.2 ± 0.2	2.2 ± 0.1
3Ni	45.0 ± 0.1	17.9 ± 0.3	20.3 ± 0.2	3.8 ± 0.1	1.3 ± 0.1	4.2 ± 0.1	4.3 ± 0.2	3.2 ± 0.2

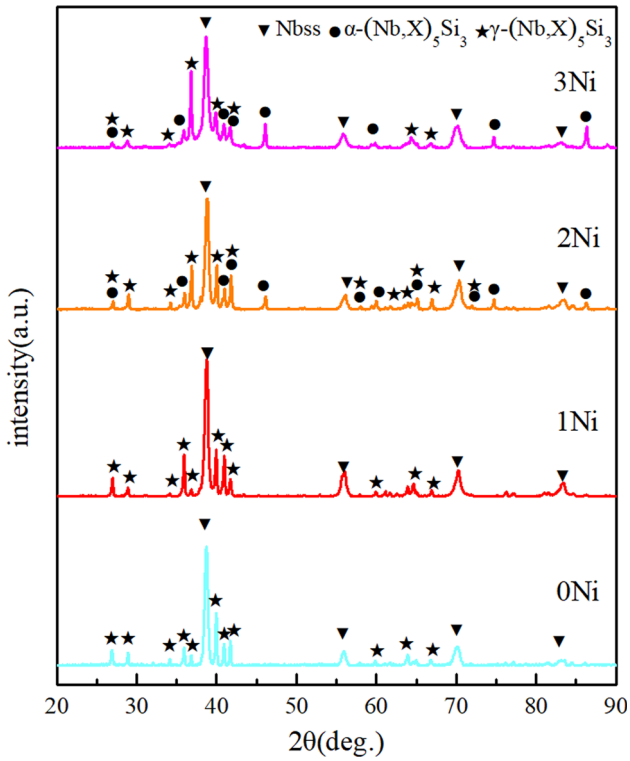

Fig. 1—XRD patterns of all alloys with different Ni contents.

phase improved the room-temperature fracture toughness.

According to Table IV, the Ni contents of the Nbss phase and γ-(Nb, X)$_5$Si$_3$ phase in the 1Ni alloy were 0.36 and 0.80 pct, respectively. The Ni content in the Nbss phase of the 2Ni alloy was also lower than that of the γ-(Nb, X)$_5$Si$_3$ phase. These results indicate that Ni was preferentially dissolved in the γ-(Nb, X)$_5$Si$_3$ phase compared to the Nbss phase. Santos *et al.*[42] studied the ternary isotherm diagram and obtained the same result.

Previous studies have shown that the Cr$_2$(Nb, X) phase easily forms a ternary eutectic structure with Nbss and silicide phases.[12,43,44] Because Cr has a low melting point, Cr solidifies last.[45] The solid solution of Ni in the Cr$_2$(Nb, X) phase was much higher than that in the other phases, reaching 16 to 18 pct, because the melting point of Ni is only 1453 °C,[46] reaching the maximum solid solubility of Nbss and silicide phases. Ni was concentrated in the liquid phase and finally dissolved in the Cr$_2$(Nb, X) phase. Therefore, the content of Ni in Cr$_2$(Nb, X) was the highest. The Ni content in the Cr$_2$(Nb, X) phase was approximately 20 pct, while the Cr content in Cr$_2$(Nb, X) decreased from 41.7 to 20 pct in the Ni-added alloys, which indicates that Ni substitutes Cr in the Cr$_2$(Nb, X) phase. There were also a few changes in the other elements with the increase in Ni, as shown in Table IV. When Ni was added to Nb–Si-based alloys, the (Cr, Ni)$_2$(Nb, X) phase appeared in the microstructure, where Cr$_2$(Nb, X) and (Cr, Ni)$_2$(Nb, X) are collectively referred to as Cr$_2$(Nb, X).

The element distribution of the 3Ni alloy was used to validate the distribution of each element in all continuous phases, as shown in Figure 3. Figure 3 shows that all other elements were segregated except Al. Thus, Nb primary formed the Nbss phase, and the content distribution from high to low was Nbss, α-(Nb, X)$_5$Si$_3$, γ-(Nb, X)$_5$Si$_3$, and Cr$_2$(Nb, X), Si formed silicide phases, Zr and Hf were primarily distributed in the silicide phase, particularly the γ-(Nb, X)$_5$Si$_3$ phase. The element distributions of Ni, Cr, and Ti were the most similar and all dissolved in the final solidified Cr$_2$(Nb, X) phase in substantial amounts, confirming the prior discussion.

Quantitative statistical analysis was performed on a large number of SEM images to calculate the area fraction of all phases, as shown in Table V and Figure 4. The area fraction of the Nbss phase gradually decreased with the increase in Ni content: the 2Ni alloy was 40.5 pct ± 5.6, and the 3Ni alloy was 34.2 pct ± 4.3. Thus, when the addition of Ni reached 2 pct, the alloy transitioned from a eutectic to hypereutectic structure. The area fraction of the α-(Nb, X)$_5$Si$_3$ phase in the 2Ni alloy was 31.9 pct ± 2.3, which increased to 38.4 pct ± 3.1 in the 3Ni alloy. In the 0Ni alloy, the content of the γ-(Nb, X)$_5$Si$_3$ phase reached 52.0 pct ± 5.7 and then decreased as the Ni concentration increased. The 3Ni alloy was only 19.2 pct ± 3.9 due to a large consumption of Si in primary α-(Nb, X)$_5$Si$_3$, leading to a marked reduction in the content of the γ-(Nb, X)$_5$Si$_3$ phase.

C. *Room-Temperature Mechanical Properties*

Figure 5 shows the average room-temperature fracture toughness (K_Q) of alloys with different Ni contents. K_Q first increased and then decreased as the Ni content increases. The room-temperature fracture toughness of the 0Ni alloy was 10.71 MPa·m$^{1/2}$. K_Q of the 2Ni alloy was the highest, reaching 12.6 MPa·m$^{1/2}$. When the Ni content reached 3 pct, K_Q dropped to 11.1 MPa·m$^{1/2}$.

Figure 6 shows the crack propagation path of the three-point bending specimens in all alloys. The four alloys exhibited a deflection in the crack propagation path, absorbing energy and increasing K_Q. Therefore, K_Q of the four alloys reached 10 MPa·m$^{1/2}$. The degree of crack deflection in each alloy is different. A significant degree of deflection increased K_Q. A detailed analysis is shown in Section 4.3. Secondary cracks were found in the 2Ni alloy, and other studies have shown that secondary cracks can reduce the driving force at the crack tip, redistributing local stress at the crack propagation tip and ultimately improving room-temperature fracture toughness.[47] Guo *et al.*[48] found the same result when adding Ta to a multielemental Nb–Si alloy.

Figure 7 shows the fracture morphology of three-point bending specimens with different Ni contents. The fracture morphology of the four alloys was composed of smooth cleavage steps and tearing ridges. With the increase in Ni content, the number of cleavage steps increased corresponding to the microstructure (Figure 2). The fracture plane of silicide phases in Figure 7(e) exhibited clear river patterns, indicating that the silicide phase was a transgranular cleavage mode. The river pattern indicate that the plasticity produced by

Table III. Lattice Parameter Values of Phases in All Alloys

Alloy	Nbss (Å)	Lattice Parameters					
		α-(Nb, X)$_5$Si$_3$			γ-(Nb, X)$_5$Si$_3$		
		a (Å)	c (Å)	c/a	a (Å)	c (Å)	c/a
0Ni	3.2908 ± 0.0019	—	—	—	7.6342 ± 0.0031	5.2193 ± 0.0029	0.6837
1Ni	3.2887 ± 0.0021	—	—	—	7.5443 ± 0.0018	5.2478 ± 0.0041	0.6956
2Ni	3.2885 ± 0.0027	6.5867 ± 0.0029	11.7976 ± 0.0055	1.7911	7.5494 ± 0.0022	5.2480 ± 0.0047	0.6952
3Ni	3.2884 ± 0.0030	6.5694 ± 0.0033	11.8597 ± 0.0049	1.8053	7.5435 ± 0.0015	5.2476 ± 0.0038	0.6957

silicide was limited,[49] and the tear ridge indicated that the Nbss phase had undergone a certain degree of plastic deformation during the fracture process, demonstrating that the ductile phase Nbss could improve room-temperature fracture toughness. The Nbss phase of the 2Ni alloy exhibited dimples between 0.2 and 0.8 μm in Figure 7(e), which was a typical ductile fracture behavior.[50] Kong and Jia[51] reported that the Nbss phase fractured through the dimple mode due to $b = a/2 \langle 111 \rangle$ active dislocations. Therefore, all alloys in this experiment exhibited brittle quasi-cleavage fractures.

Figure 8 shows the surface morphology measurements of three-point bending fractures with different Ni contents. The quantitative calculation of the surface area and specific surface area (ratio of surface area to projected area) of each alloy obtained by three-point bending specimens are listed in Table VI. The 2Ni alloy had the largest specific surface area of 2.776, which means that the 2Ni alloy had the most undulations. Conversely, the fracture surface of the 0Ni alloy was the flattest.

Figure 9 shows the room-temperature compressive strength of alloys with different Ni contents. The 0Ni alloy had the lowest maximum compressive strength (only 1976 MPa). The maximum compressive strength value of 1Ni alloy is 2116 MPa, which gradually decreased to 2046 MPa as the Ni concentration increased.

IV. DISCUSSION

A. *Effect of Ni Addition on Microstructure Evolution*

The 0Ni alloy was composed of Nbss, the γ-(Nb, X)$_5$Si$_3$ phase, and the Cr$_2$(Nb, X) phase (Figures 2(a) and (b)). According to the binary Nb–Si phase diagram,[52] the eutectic point of the Nb–Si alloy was 18.7 pct. Ma and Guo[53] reported that the addition of Zr and Mo could move the eutectic point of a Nb–Si alloy in the direction of the low Si content, and make the hypoeutectic alloy (Nb–22Ti–15Si–5Cr–3Al–2Hf) become a hypereutectic alloy. Zelenitsas and Tsakiropoulos[27] and Li *et al.*[54] showed that Al and Cr elements transform hypoeutectic Nb–Si alloy into a hypereutectic alloy, respectively. In this study, the addition of Zr, Al, and Cr in the 0Ni alloy moved the eutectic point of the Nb–Si alloy in the direction of a low Si content, resulting in a eutectic rather than a hypoeutectic structure. The silicide phase in the base alloy (0Ni) was γ-(Nb, X)$_5$Si$_3$ instead of α-(Nb, X)$_5$Si$_3$ or β-(Nb, X)$_5$Si$_3$ phase, primarily due to the content of Zr, Hf, and Ti in the alloy. These elements and Si easily formed Zr$_5$Si$_3$ (P6$_3$/mcm), Hf$_5$Si$_3$ (P6$_3$/mcm), and Ti$_5$Si$_3$ (P6$_3$/mcm) phases with the same lattice structure as the γ-(Nb, X)$_5$Si$_3$ (P6$_3$/mcm)phase. Several studies have demonstrated that Zr, Hf, and Ti elements are distributed in large amounts in the silicide phase, which promotes the formation of the γ-(Nb, X)$_5$Si$_3$ phase.[12,35,55]

Analyzing the Nb–Si binary phase diagram shows two ways to precipitate the α-(Nb, X)$_5$Si$_3$ phase; one is obtained by the hypoeutectic or eutectic structure through the eutectoid decomposition reaction of Nb$_3$Si. For example, Kommineni *et al.*[33] reported that Zr can promote the eutectoid decomposition reaction of Nb$_3$Si to form the α-(Nb, X)$_5$Si$_3$ phase. The other is the hypereutectic structure, which includes the primary α-(Nb, X)$_5$Si$_3$ phase through the peritectoid reaction between Nb$_3$Si and the primary β-(Nb, X)$_5$Si$_3$ phase. The difference between the two α-(Nb, X)$_5$Si$_3$ is the phase size. The size of α-(Nb, X)$_5$Si$_3$ in the eutectoid decomposition reaction is small, while the primary α-(Nb, X)$_5$Si$_3$ phase is more than 20 μm. The primary α-(Nb, X)$_5$Si$_3$ phase (Figure 2(e)) appears in the 2Ni alloy. With the increase in Ni content, the primary α-(Nb, X)$_5$Si$_3$ phase in the 3Ni alloy continues to grow and the length can reach 200 μm. Thus, 2Ni and 3Ni alloys are primary α-(Nb, X)$_5$Si$_3$ phases instead of eutectoid-decomposed α-(Nb, X)$_5$Si$_3$.

Because the Cr$_2$(Nb, X) phase has a low melting point, it solidifies the latest.[56] With the increase in Ni content, the undissolved Ni also dissolves in the Cr$_2$(Nb, X) phase to form Ni-rich Cr$_2$(Nb, X), increasing the area fraction. Therefore, the Cr$_2$(Nb, X) phase content of the 3Ni alloy reaches 8 pct.

Thus, the phase evolution sequences of multielemental Nb–Si alloys with different Ni contents can be written as follows (Figure 10):

0Ni and 1Ni alloys:

(i) L $\rightarrow$ Nbss + (Nb, X)$_3$Si
$\rightarrow$ Nbss + γ-(Nb, X)$_5$Si$_3$
$\rightarrow$ Nbss + γ-(Nb, X)$_5$Si$_3$ + Cr$_2$(Nb, X).

2Ni and 3Ni alloy:

(ii) L $\rightarrow$ primary α-(Nb, X)$_5$Si$_3$ + L$_1$
$\rightarrow$ primary α-(Nb, X)$_5$Si$_3$ + ((Nb, X)$_3$Si/Nbss)$_{\text{Eutectoid}}$

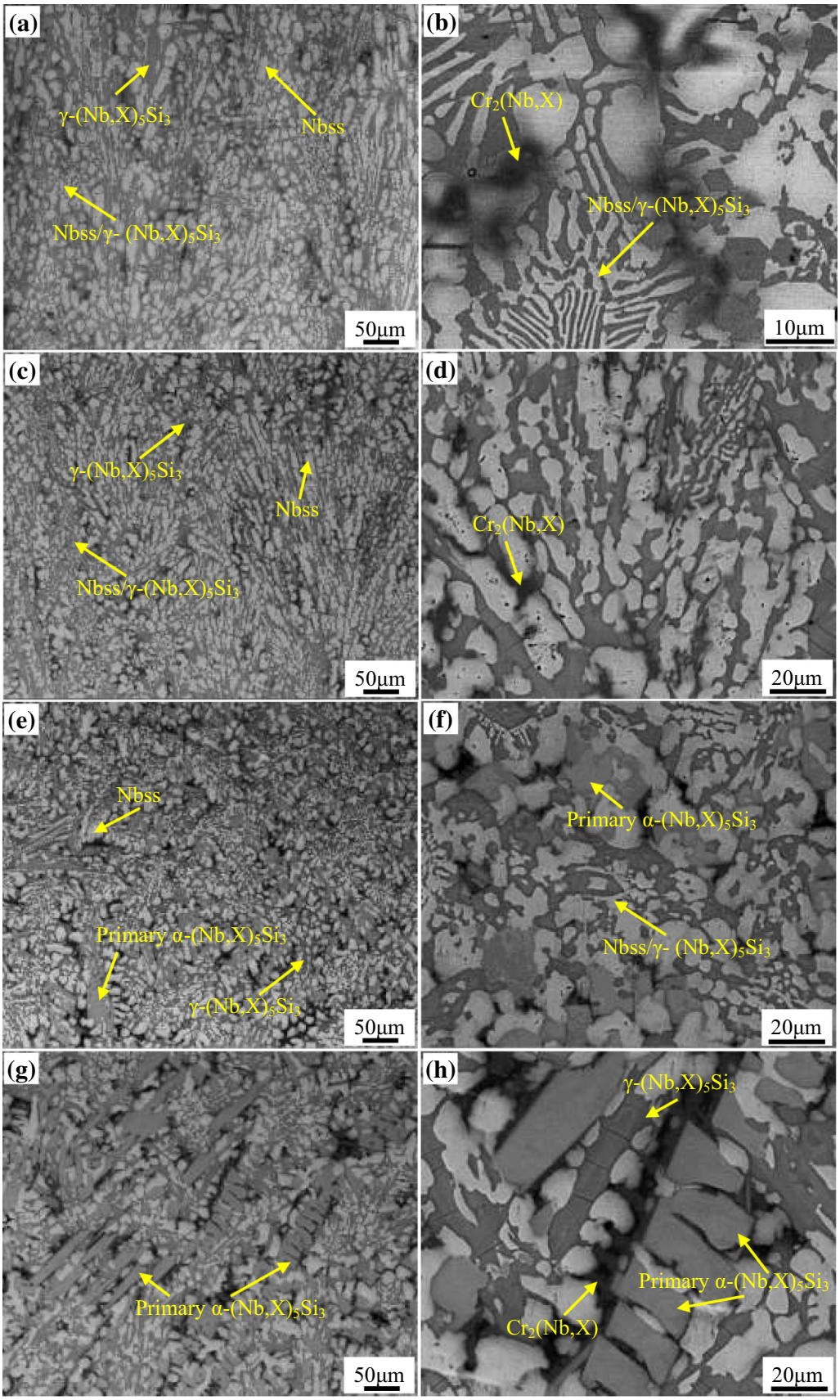

Fig. 2—BSE images of the microstructure in the multielement Nb–Si alloy with different Ni contents: (*a*) and (*e*) 0Ni, (*b*) and (*f*) 1Ni, (*c*) and (*g*) 2Ni, and (*d*) and (*h*) 3Ni.

Table IV. Chemical Compositions of Phases in All Alloys With Different Ni Contents

Alloy	Phase	Compositions							
		Nb	Si	Ti	Cr	Al	Hf	Zr	Ni
0Ni	Nbss	62.2 ± 2.1	7.4 ± 0.2	16.9 ± 0.5	4.4 ± 0.2	1.2 ± 0.1	2.5 ± 0.5	5.4 ± 0.2	—
	γ-(Nb, X)$_5$Si$_3$	25.6 ± 0.9	39.7 ± 1.9	16.1 ± 0.6	1.7 ± 0.1	0.8 ± 0.1	6.1 ± 0.4	9.0 ± 0.4	—
	Cr$_2$(Nb, X)	18.8 ± 0.8	5.7 ± 0.3	19.2 ± 0.6	41.7 ± 2.3	1.0 ± 0.2	7.4 ± 0.6	6.2 ± 0.7	—
1Ni	Nbss	61.5 ± 2.3	7.3 ± 1.1	17.1 ± 0.5	4.7 ± 0.3	1.2 ± 0.2	2.4 ± 0.2	5.5 ± 0.9	0.4 ± 0.1
	γ-(Nb, X)$_5$Si$_3$	22.3 ± 1.2	41.2 ± 2.6	18.6 ± 0.7	1.1 ± 0.2	2.2 ± 0.2	5.8 ± 0.3	8.1 ± 0.6	0.8 ± 0.1
	Cr$_2$(Nb, X)	18.5 ± 0.3	8.9 ± 0.7	20.1 ± 1.0	23.6 ± 2.6	0.9 ± 0.2	5.8 ± 0.4	5.9 ± 0.7	16.4 ± 0.6
2Ni	Nbss	61.0 ± 1.8	6.6 ± 0.8	17.6 ± 1.6	5.5 ± 1.0	1.3 ± 0.1	2.0 ± 0.1	5.3 ± 0.5	0.7 ± 0.1
	γ-(Nb, X)$_5$Si$_3$	25.6 ± 1.1	43.6 ± 2.1	15.7 ± 1.2	0.9 ± 0.2	2.2 ± 0.3	5.9 ± 0.3	5.4 ± 0.2	0.7 ± 0.1
	α-(Nb, X)$_5$Si$_3$	38.6 ± 1.3	37.4 ± 1.7	9.8 ± 0.6	0.7 ± 0.1	0.5 ± 0.1	4.9 ± 0.6	6.7 ± 0.2	1.5 ± 0.1
	Cr$_2$(Nb, X)	11.9 ± 0.7	6.5 ± 0.4	27.3 ± 1.8	18.2 ± 1.0	4.4 ± 0.1	6.3 ± 0.7	6.4 ± 0.4	18.2 ± 0.3
3Ni	Nbss	61.7 ± 2.6	6.5 ± 0.1	17.9 ± 1.8	4.4 ± 0.5	1.6 ± 0.2	2.0 ± 0.3	5.0 ± 0.4	0.8 ± 0.1
	α-(Nb, X)$_5$Si$_3$	39.6 ± 1.7	36.9 ± 1.3	10.0 ± 0.9	0.8 ± 0.1	0.2 ± 0.1	4.6 ± 0.3	5.5 ± 0.2	2.4 ± 0.2
	γ-(Nb, X)$_5$Si$_3$	23.7 ± 0.8	42.5 ± 1.0	14.9 ± 1.2	0.6 ± 0.1	2.1 ± 0.2	6.1 ± 0.8	9.0 ± 0.3	1.2 ± 0.1
	Cr$_2$(Nb, X)	12.3 ± 0.4	7.5 ± 0.2	24.7 ± 1.8	22.1 ± 1.4	4.4 ± 0.2	6.1 ± 0.5	5.7 ± 0.1	17.2 ± 0.7

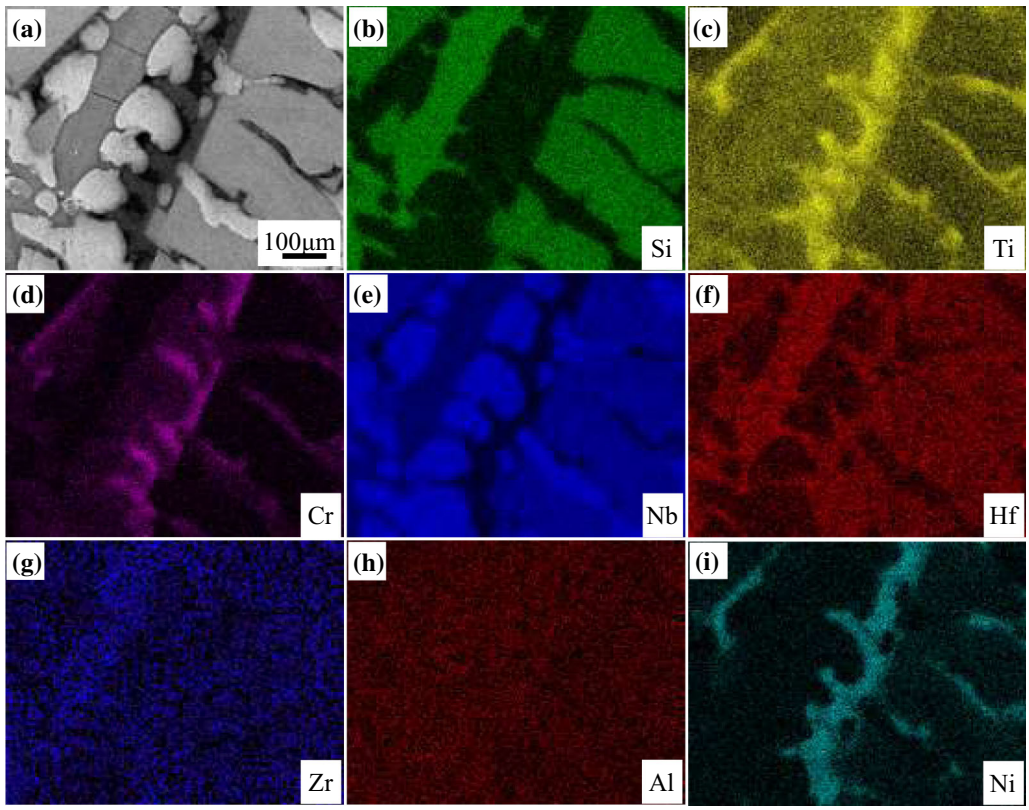

Fig. 3—Elemental X-ray mapping of fine eutectic in 3Ni alloy: (*a*) BSE image, (*b*) Si, (*c*) Ti, (*d*) Cr, (*e*) Nb, (*f*) Hf, (*g*) Zr, (*h*) Al, and (*i*) Ni.

→ primary α-(Nb, X)$_5$Si$_3$ + (Nbss/γ-(Nb, X)$_5$Si$_3$)$_{Eutectoid}$

→ primary α-(Nb, X)$_5$Si$_3$ + (Nbss/γ-(Nb, X)$_5$Si$_3$)$_{Eutectoid}$ + Cr2(Nb, X).

Figure 10 shows a schematic diagram of the phase evolution sequence of all alloys with different Ni contents. The solidification sequence of the 0Ni and 1Ni alloys was similar, and the primary difference between the 3Ni and 2Ni alloys was that the 3Ni alloy had a larger primary α-(Nb, X)$_5$Si$_3$ phase and a higher content of the Cr$_2$(Nb, X) phase.

B. *Effect of Ni Addition on Mechanical Performance*

The low room-temperature fracture toughness limits the application of Nb–Si alloys.[1,34] K_Q of the 1Ni alloy was marginally increased by 3.3 pct compared to that of the 0Ni alloy (Figure 5), primarily because (1) the

Table V. Area Fraction (Pct) of Microstructure Constituents in All Alloys With Different Ni Contents

Alloy	Phase			
	Nbss	α-(Nb, X)$_5$Si$_3$	γ-(Nb, X)$_5$Si$_3$	Cr$_2$(Nb, X)
0Ni	44.8 ± 4.5	0	52.0 ± 5.7	3.2 ± 0.4
1Ni	44.1 ± 3.1	0	50.9 ± 6.3	5.0 ± 1.4
2Ni	40.5 ± 5.6	31.9 ± 2.3	20.9 ± 4.9	6.7 ± 1.6
3Ni	34.2 ± 4.3	38.4 ± 3.1	19.2 ± 3.9	8.0 ± 2.8

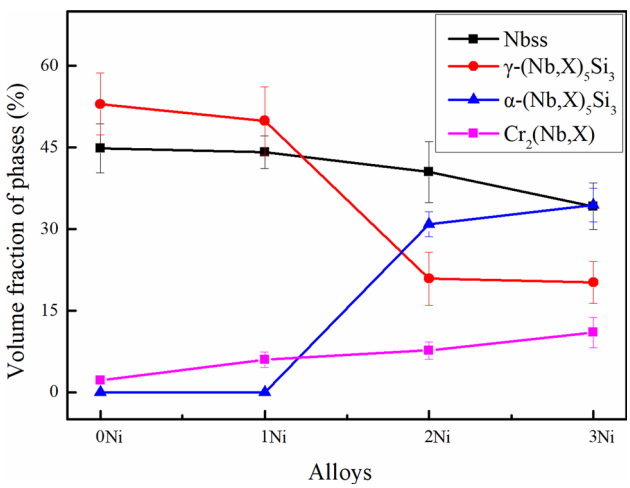

Fig. 4—Area fraction of microstructure constituents in all alloys with different Ni contents.

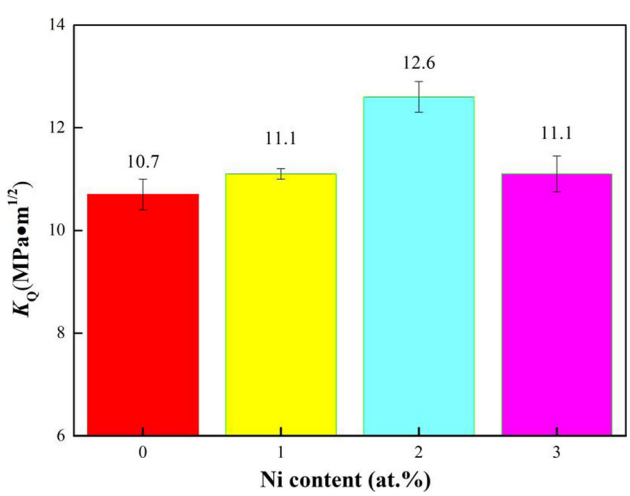

Fig. 5—Average room-temperature fracture toughness (K_Q) of alloy with different Ni contents.

addition of Ni made the 'c' axis of the γ-(Nb, X)$_5$Si$_3$ phase longer and the 'a' axis shorter, and (2) the c/a value increased from 0.6837 to 0.6956 (Table III). Hexagonal intermetallic compounds are known to have few slip systems due to their high intrinsic brittleness. Wang *et al.*[41] demonstrated that alloying elements could modify the lattice constant of the silicide phase. When the lattice constant of the silicide phase was near 1, the plastic deformability of the silicide phase was higher.

The type of silicide present is known to have a strong impact on room-temperature fracture toughness.[9] Compared with the hexagonal γ-(Nb, X)$_5$Si$_3$ phase, the tetragonal α-(Nb, X)$_5$Si$_3$ phase was more beneficial to room-temperature fracture toughness.[57] Although the silicide content of the 2Ni and 3Ni alloys was higher than that of the 0Ni and 1Ni alloys, the majority of silicide phases was α-(Nb, X)$_5$Si$_3$, and the content of the γ-(Nb, X)$_5$Si$_3$ phase decreased from more than 50 pct to approximately 20 pct, resulting in a higher K_Q for the 2Ni and 3Ni alloys.

After the crack propagated from the silicide to the Nbss phase, the stress field at the crack tip tended to connect with the silicide phase closest to the crack.[19,22,26] If the silicide phase was not on the extension line of the crack propagation, deflection would occur, but when the size of the primary phase was too large (> 100 μm), the crack passed straight through, reducing deflection. To a certain extent, the small-sized primary silicide phase could be used as the origin of cracks, forming secondary cracks or inducing crack propagation. Sun *et al.*[13] showed that a certain size of silicide phase can change the orientation of the crack propagation. Thus, K_Q of the 2Ni alloy was the highest, and K_Q of the 3Ni alloy decreased to 11.14 MPa·m$^{1/2}$.

The deflection path and deflection of the crack are closely related to the room-temperature fracture toughness, which means that the greater the deflection is, the higher the fracture toughness value is.[58] In Figure 6, the crack growth image is quantified, and the crack growth path is measured, where 1 pixel equals 1 μm. Then, the measured pixel positions were connected to create a curve, as shown in Figure 11. The curve was fitted to a straight line using the least square method; the degree of fit 'R' (linear correlation coefficient) was determined; and 'D' was the deflection of the curve (*i.e.*, the reciprocal of the R value). The smaller the R value and the higher the D value are, the more tortuous the crack propagation path. R and D of the four alloys are listed in Table VII. D of the 2Ni was 4.17, and D of 0Ni was only 1.03, indicating that the cracks in the 2Ni alloy had more bends and consumed more energy during propagation. R and K_Q exhibit the same trends in this study, indicating that the degree of crack bending influenced the room-temperature fracture toughness.

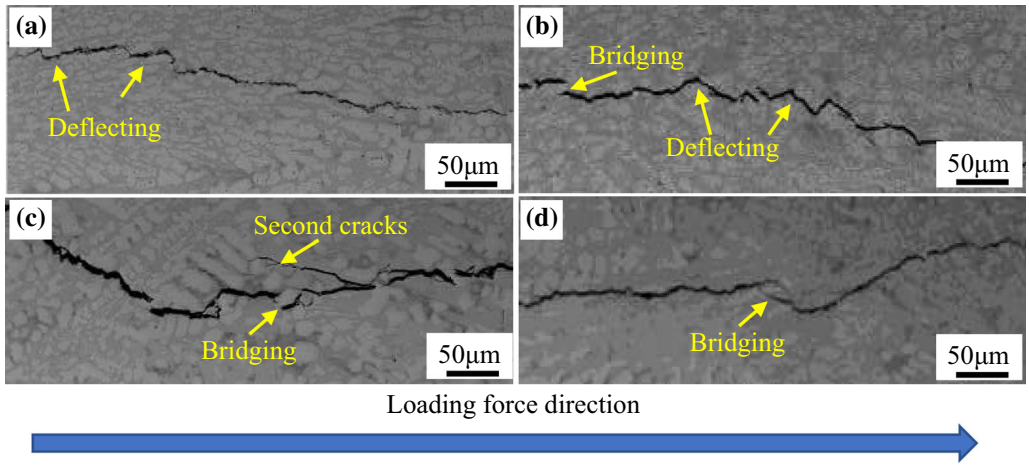

Fig. 6—BSE images of crack propagation paths in all alloys with different Ni contents: (*a*) 0Ni, (*b*) 1Ni, (*c*) 2Ni, and (*d*) 3Ni.

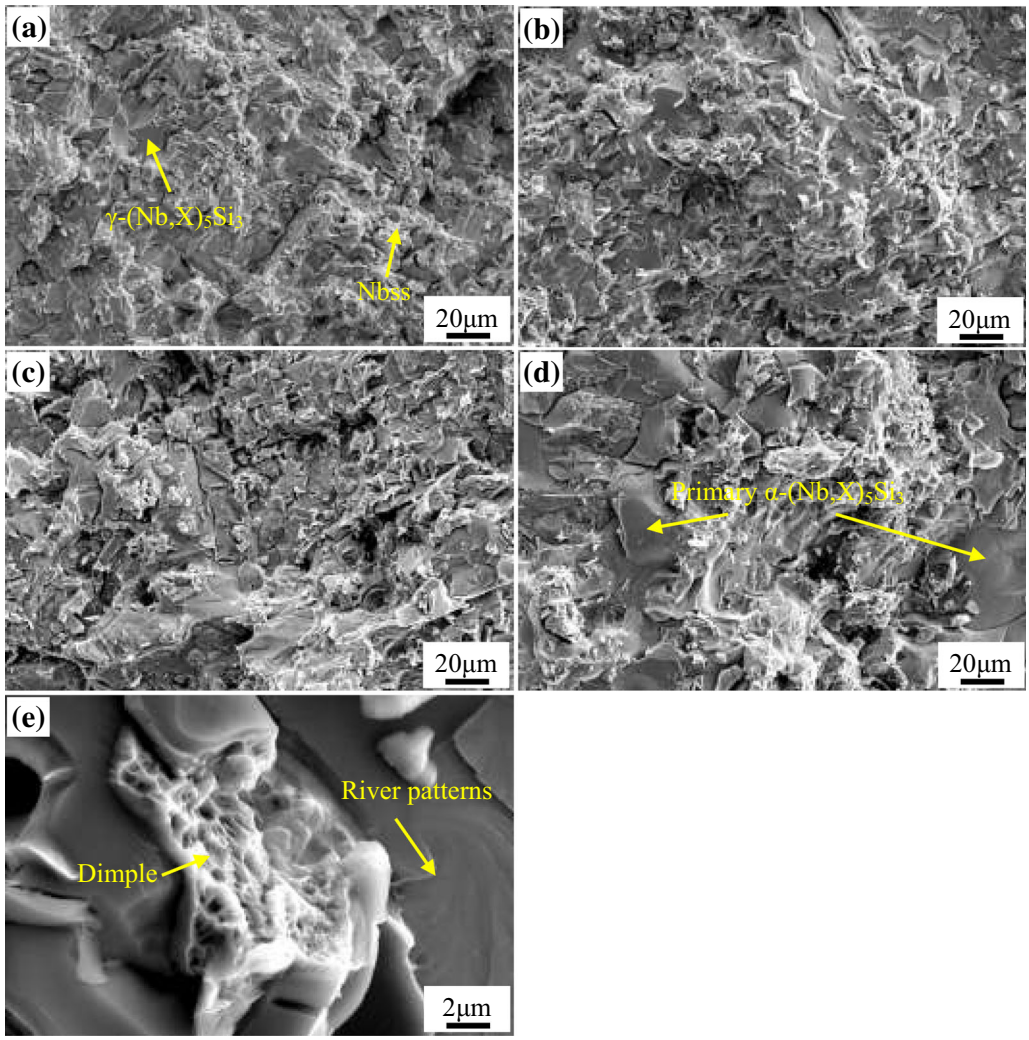

Fig. 7—Fractographies of the three-point bending specimens in all alloys with different Ni contents: (*a*) 0Ni, (*b*) 1Ni, (*c*) 2Ni, (*d*) 3Ni, and (*e*) is magnification of 2Ni alloy.

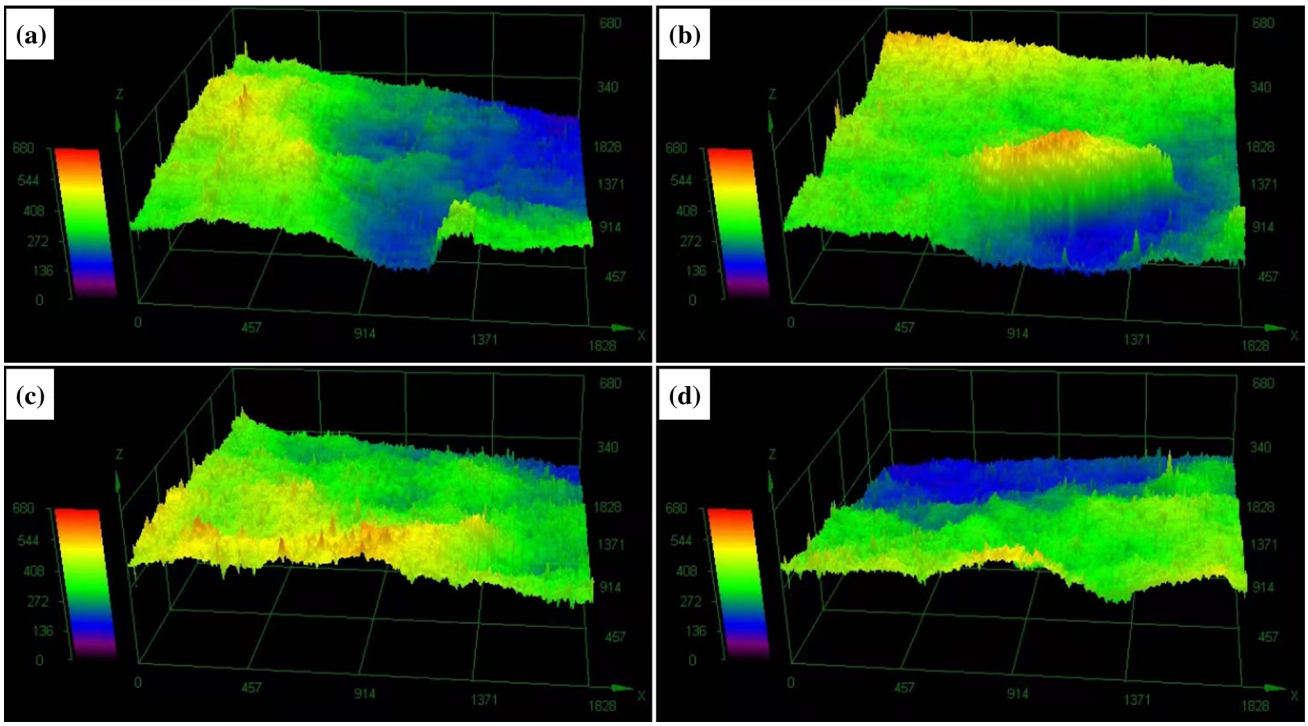

Fig. 8—3D surface morphology measurements with three-point bending test samples: (*a*) 0Ni, (*b*)1Ni, (*c*) 2Ni, and (*d*) 3Ni.

Table VI. Surface Area and Specific Surface Area of the Fracture Surface for Three-Point Bending Specimens

Alloy	Surface Area (μm^2)	Projected Area (μm^2)	Specific Surface Area (S/M)
0Ni	8,315,715	3,343,673	2.487
1Ni	8,703,581	3,343,673	2.603
2Ni	9,282,036	3,343,673	2.776
3Ni	8,957,700	3,343,673	2.679

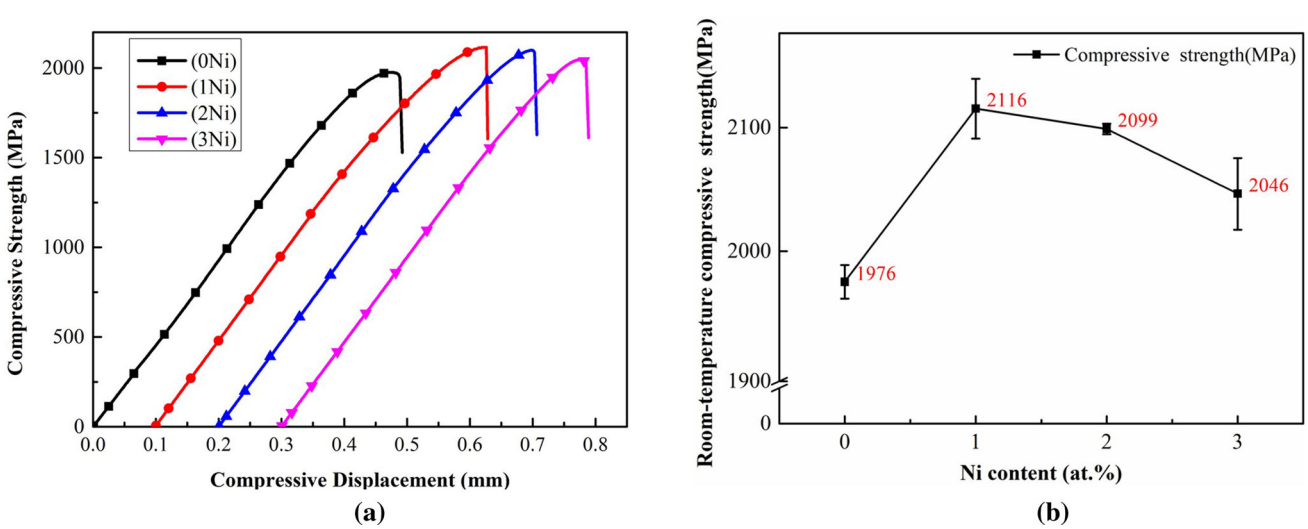

Fig. 9—Room-temperature compression strength of all alloys with different Ni contents: (*a*) representative compressive strength–displacement curves, and (*b*) compressive strength.

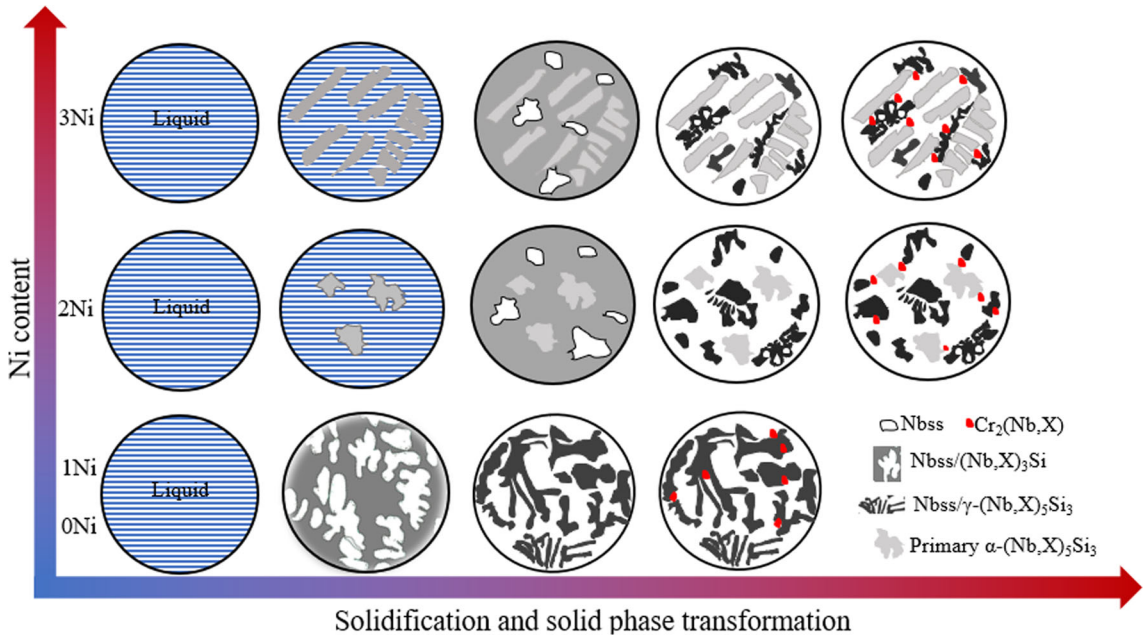

Fig. 10—Schematic diagram of the phase evolution sequence of all alloys with different Ni contents.

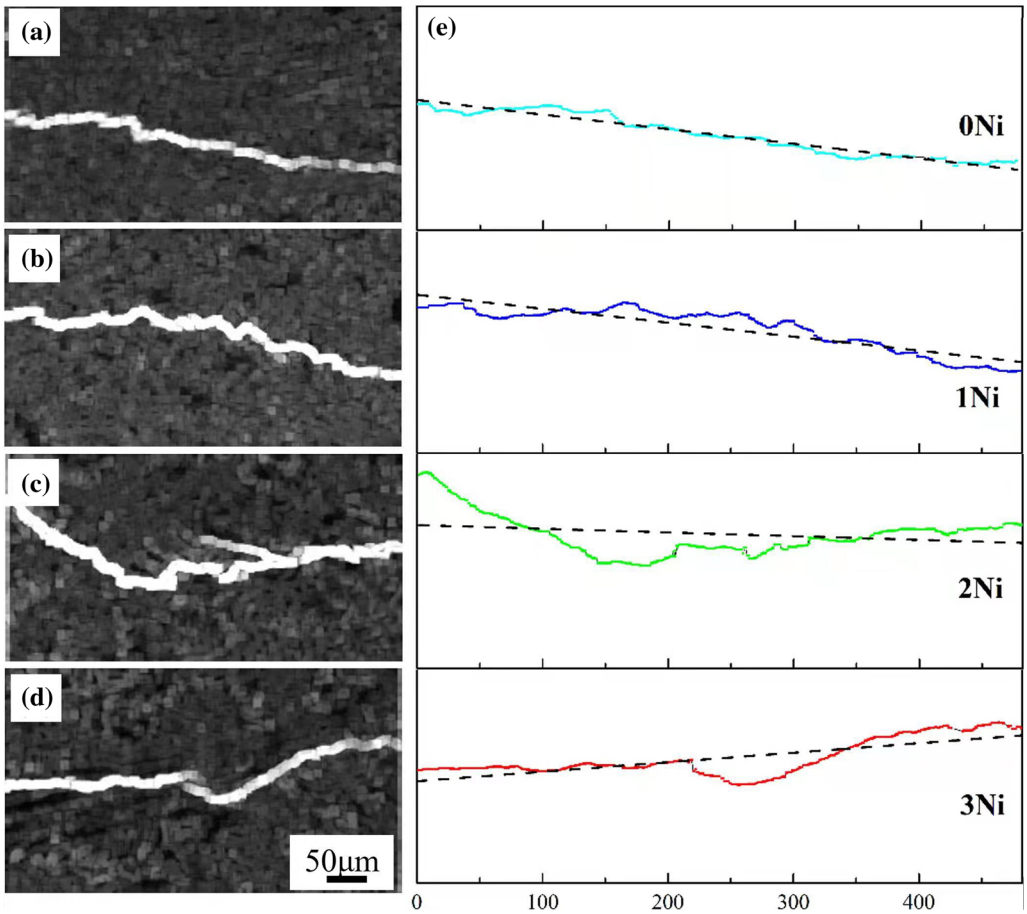

Fig. 11—Pixel map of crack growth paths and curves of the simulated propagation path: (*a*) 0Ni, (*b*) 1Ni, (*c*) 2Ni, (*d*) 3Ni, and (*e*) simulated propagation path of all alloys.

Table VII. Quantitative Deflection Degrees of the Alloys

Alloy	0Ni	1Ni	2Ni	3Ni
R	0.97	0.90	0.24	0.73
D (1/R)	1.03	1.11	4.17	1.37

Ni was dissolved in the Nbss phase to produce a solid solution strengthening effect and to increase the maximum compressive strength. Sankar *et al.*[35] showed that adding 3 at. pct Ni to a Nb–Si alloy increased the microhardness of the Nbss phase from 454 to 582 Hv. Therefore, the maximum compressive strength of the 1Ni alloy was higher than that of the 0Ni alloy. The literature also indicated that the microhardness of the γ-(Nb, X)$_5$Si$_3$ phase is higher than that of the α-(Nb, X)$_5$Si$_3$ phase.[44]. Because the silicide phase of the 2Ni and 3Ni alloys was primary α-(Nb, X)$_5$Si$_3$, their maximum compressive strength was marginally lower than that of the 1Ni alloys, as shown in Section III–B. Compared with the Nbss phase, the silicide phase was more conducive to improving room-temperature and high-temperature strength. Zelenitsas and Tsakiropoulos[29] showed that when the silicide content in the binary Nb–Si alloy increases from 28 to 38 pct, the room-temperature bending strength increased from 480 to 500 MPa. Li and Peng[59] found that with the increase in silicide content, the room-temperature compressive strength increased from 947 to 1080 MPa in a Nb–(11, 16, 18) Si–6Ti alloy. Therefore, the maximum compressive strength of the 2Ni and 3Ni alloys in this study was higher than that of the 0Ni alloys. Thus, the highest compressive strength of the 1Ni alloy can be attributed to the solid solution strengthening of Ni and the high content of the γ-(Nb, X)$_5$Si$_3$ phase.

V. CONCLUSIONS

The effects of varying Ni concentrations on the microstructure, room-temperature fracture toughness, and compressive strength of Nb–Si alloy were thoroughly investigated based on the seven-elemental alloy (Nb–Si–Ti–Cr–Al–Hf–Zr). The primary conclusions of this study are as follows:

(1) 0Ni and 1Ni alloys were composed of Nbss, γ-(Nb, X)$_5$Si$_3$ and Cr$_2$(Nb, X) phases. 2Ni and 3Ni alloys were composed of primary α-(Nb, X)$_5$Si$_3$, Nbss, γ-(Nb, X)$_5$Si$_3$, and Cr$_2$(Nb, X) phases. The eutectic Nb–Si alloy became a hypereutectic Nb–Si alloy as the Ni concentration increased.

(2) With the increase in Ni content, K_Q first increased and then decreased. The highest K_Q of the 2Ni alloy was 12.6 MPa·m$^{1/2}$. The high content of α-(Nb, X)$_5$Si$_3$ (low content of γ-(Nb, X)$_5$Si$_3$) increased K_Q, while the bulk primary α-(Nb, X)$_5$Si$_3$ phase decreased K_Q.

(3) The room-temperature maximum compressive strength first increased and then decreased with more Ni. The maximum compressive strength of the 1Ni alloy was 2116 MPa, and the strengthening mechanism was solid solution strengthening of Ni and a high content of the γ-(Nb, X)$_5$Si$_3$ phase.

ACKNOWLEDGMENTS

The authors gratefully acknowledge support from the National Natural Science Foundation of China (51825401) and Young Scientist Studio of Harbin Institute of Technology.

CONFLICT OF INTEREST

On behalf of all authors, the corresponding author states that there is no conflict of interest or personal relationships that could have appeared to influence the work reported in this paper. The authors declare the following financial interests/personal relationships which may be considered as potential competing interests.

REFERENCES

1. P. Tsakiropoulos: *J. Alloys Compd.*, 2018, vol. 748, pp. 569–76.
2. B.P. Bewley, M.R. Jackson, and J.C. Zhao: *MRS Bull.*, 2003, vol. 28, pp. 636–46.
3. M.G. Mendiratta, J.J. Lewandowski, and D.M. Dimiduk: *Metall. Mater. Trans. A*, 1991, vol. 22A, pp. 1573–83.
4. I. Papadimitriou, C. Utton, and P. Tsakiropoulos: *Sci. Technol. Adv. Mater.*, 2017, vol. 18, pp. 467–79.
5. G. Tai, C. Li, and B. Jing: *Intermetallics*, 2009, vol. 34, pp. 363–76.
6. Y.X. Tian, J.T. Guo, and L.Y. Sheng: *Intermetallics*, 2008, vol. 16, pp. 807–12.
7. Y. Sainan, J. Lina, and S. Linfen: *Intermetallics*, 2013, vol. 38, pp. 102–06.
8. B.P. Bewley, S.D. Sitzman, and L.N. Brewer: *Microsc. Microanal.*, 2004, vol. 10, pp. 470–80.
9. Y.H. Duan: *Rare Met. Mater. Eng.*, 2015, vol. 44, pp. 18–23.
10. D.Z. Chen, Q. Wang, and R.R. Chen: *Mater. Charact.*, 2021, vol. 182, p. 111563.
11. S. Zhang and X.P. Guo: *Intermetallics*, 2016, vol. 70, pp. 33–44.
12. S. Zhang and X.P. Guo: *Mater. Sci. Eng. A*, 2015, vol. 638, pp. 121–31.
13. G.X. Sun, L.N. Jia, and C.T. Ye: *Intermetallics*, 2021, vol. 133, p. 107172.
14. W.Y. Kim, H. Tanaka, and A. Kasama: *Intermetallics*, 2001, vol. 9, pp. 827–34.
15. Z.F. Li and P. Tsakiropoulos: *Intermetallics*, 2010, vol. 18, pp. 1072–78.
16. K.S. Chan: *Mater. Sci. Eng. A*, 2002, vol. 329, pp. 513–22.
17. E.Y. Guo and S.S. Sudhanshu: *Mater. Sci. Eng. A*, 2017, vol. 687, pp. 99–106.
18. K.S. Chan: *Metall. Mater. Trans. A*, 2003, vol. 34A, pp. 2315–28.
19. D.L. Davidson and K.S. Chan: *Metall. Mater. Trans. A*, 1999, vol. 30A, pp. 2007–18.
20. S.M. Zhang, J.R. Zhou, and J.B. Sha: *Intermetallics*, 2015, vol. 57, pp. 146–55.
21. K.S. Chan: *Mater. Sci. Eng. A*, 2002, vol. 337, pp. 59–66.
22 K.S. Chan and D.L. Davidson: *Metall. Mater. Trans. A*, 2003, vol. 34A, pp. 1833–49.

23. W. Wang, B. Zhang, and C. Zhou: *Corros. Sci.*, 2014, vol. 86, pp. 304–09.
24 Y. Murayama and S. Hanada: *Sci. Technol. Adv. Mater.*, 2002, vol. 3, pp. 145–56.
25. J. Sha, C. Yang, and J. Liu: *Scripta Mater.*, 2010, vol. 62, pp. 859–62.
26. K.S. Chan: *Metall. Mater. Trans. A*, 2003, vol. 34A, pp. 1833–49.
27. K. Zelenitsas and P. Tsakiropoulos: *Mater. Sci. Eng. A*, 2006, vol. 416, pp. 269–80.
28. T. Murakami, S. Sasaki, and K. Ichikawa: *Intermetallics*, 2001, vol. 9, pp. 629–35.
29. K. Zelenitsas and P. Tsakiropoulos: *Intermetallics*, 2005, vol. 13, pp. 1079–95.
30. S. Kashyap, C.S. Tiwary, and K. Chattopadhyay: *Mater. Sci. Eng. A*, 2013, vol. 559, pp. 74–85.
31. Z.P. Sun, J.M. Guo, and Z. Chen: *Rare Met. Mater. Eng.*, 2016, vol. 45, pp. 1678–82.
32. G. Kommineni, B.R. Golla, and Z. Alam: *J. Alloys Compd.*, 2021, vol. 873, p. 159832.
33. G. Kommineni, A.M. Zafir, and R. Sarkar: *Mater. Charact.*, 2020, vol. 171, p. 110723.
34. Y. Li, X. Lin, and Y. Hu: *J. Alloys Compd.*, 2019, vol. 783, pp. 66–76.
35. M. Sankar, G. Phanikumar, and V. Prasad: *Mater. Sci. Eng. A*, 2019, vol. 754, pp. 224–31.
36. K. Geethasree, V. Prasad, and G.B. Raju: *Corros. Sci.*, 2019, vol. 148, pp. 293–306.
37. M. Sankar, G. Phanikumar, and V. Prasad: *Mater. Today Proc.*, 2016, vol. 3, pp. 3094–3103.
38. S. Miura, T. Hatabata, and T. Okawa: *Metall. Mater. Trans. A*, 2014, vol. 45A, pp. 1136–47.
39. ASTM International: *Standard Test Method for Linear-Elastic Plane-Strain Fracture Toughness KIc of Metallic Materials: ASTM E399-12*, ASTM, West Conshohocken, 2012.
40. A. Takeuchi and A. Inoue: *Mater. Trans.*, 2005, vol. 46, pp. 2817–29.
41. Q. Wang, T.Y. Zhao, and R.R. Chen: *Mater. Sci. Eng. A*, 2021, vol. 804, p. 140789.
42. V.O.D. Santos, H.M. Petrilli, and L. Eleno: *CALPHAD-Comput. Coupling Phase Diagr. Thermochem.*, 2015, vol. 51, pp. 57–66.
43. F. Gang, A. Kauffmann, and M. Heilmaier: *Metall. Mater. Trans. A*, 2018, vol. 49A, pp. 763–71.
44. S. Zhang, L. Wei, and J. Sha: *Prog. Nat. Sci.*, 2018, vol. 28, pp. 96–104.
45. S. Zhang and X.P. Guo: *Intermetallics*, 2015, vol. 57, pp. 83–92.
46. G. Qin, R.R. Chen, and P.K. Liaw: *Nanoscale*, 2020, vol. 12, pp. 3965–76.
47. N. Sekido, Y. Kimura, and S. Miura: *J. Alloys Compd.*, 2006, vol. 425, pp. 223–29.
48. Y. Guo, L. Jia, and B. Kong: *Intermetallics*, 2017, vol. 92, pp. 1–6.
49. R.M. Nekkanti and D.M. Dimiduk: *Mater. Res. Soc. Symp. Proc.*, 1990, vol. 194, pp. 175–82.
50. R.W. Armstrong: *Eng. Fract. Mech.*, 1987, vol. 28, pp. 529–38.
51. B. Kong and L.N. Jia: *Adv. Eng. Mater.*, 2017, vol. 19, p. 1700442.
52. M.E. Schlesinger, H. Okamoto, and A.B. Gokhale: *J. Phase Equilib.*, 1993, vol. 14, pp. 502–09.
53. R. Ma and X.P. Guo: *J. Alloys Compd.*, 2021, vol. 870, p. 159437.
54. Y. Li, C. Li, and Z. Du: *CALPHAD-Comput. Coupling Phase Diagr. Thermochem.*, 2013, vol. 43, pp. 112–23.
55 S. Zhang and X. Guo: *Intermetallics*, 2015, vol. 64, pp. 51–58.
56 Y. Qiao, X.P. Guo, and Y Zeng. *Intermetallics*, 2017, vol. 88, pp. 19–27.
57. M. Xiao, X.P. Guo, and M. Fu: *Intermetallics*, 2018, vol. 98, pp. 11–17.
58. Y. Wang, L. Jia, and G. Sun: *Int. J. Refract. Met. Hard Mater.*, 2020, vol. 94, p. 105359.
59. Z. Li and L.M. Peng: *Acta Mater.*, 2007, vol. 55, pp. 6573–85.

Publisher's Note Springer Nature remains neutral with regard to jurisdictional claims in published maps and institutional affiliations.